

Measurements of Seismometer Orientation of the First Phase CHINArray and Their Implications on Vector-Recording-Based Seismic Studies

Sijia Zeng^{1,2,3}, Yong Zheng^{*2}, Fenglin Niu⁴, and Sanxi Ai²

ABSTRACT

From 2011 to 2013, the CHINArray project led by the Institute of Geophysics, China Earthquake Administration, made the first phase deployment of 350 broadband seismometers at the southeastern margin of the Tibetan plateau. The three-component records of the CHINArray-I have been widely used in studying seismic structures beneath the margin under the assumption that the two horizontal components of seismometers are well aligned toward geographic north and east. In this study, we estimated the actual orientation of the two horizontal components of the 350 seismometers by analyzing *P*-wave particle motions of teleseismic earthquakes. Among the 350 stations, we found 80 stations were mildly misaligned by 5°–20°, and another 49 stations had misorientations larger than 20° or other malfunctioning issues. We also investigated how sensor misalignment affects seismic studies that rely on the vectorial nature of seismic recording, such as constructing receiver functions, estimating seismic anisotropy, and extracting surface wave Green's functions from ambient-noise data. We found a large deviation in sensor orientation could result in wrong results or large measurement errors, whereas a mild sensor misalignment tended to decrease measurement stability and reliability.

KEY POINTS

- Many ChinArray stations were significantly misaligned during installation.
- We have determined the station orientations and documented several instrumentation problems.
- Seismic studies using ChinArray data can benefit by correcting for the demonstrated misalignments.

Supplemental Material

INTRODUCTION

The Yunnan and Sichuan provinces at the southeastern margin of the Tibetan plateau make up one of the most earthquake-prone areas on the Earth. This is also a part of a north–south elongated band in central part of China, known as the north–south earthquake belt (NSEB). Because of the high seismicity and the large surface deformation, the margin has been a natural laboratory for studies of key scientific questions, such as seismogenic processes of large continental earthquakes, lithospheric structures, orogenic processes, and deformation mechanisms (Royden *et al.*, 1997; Liu and Yang, 2003; Bai *et al.*, 2010; Yin, 2010; Z. Xie *et al.*, 2013; Zhang, 2013; Zhang and Engdahl, 2013). In fact, many seismic studies have been conducted regarding this region using data recorded by

permanent China Earthquake Administration (CEA) stations and a couple of Portable Array Seismic Studies of the Continental Lithosphere temporary deployments (Yao *et al.*, 2008; Yang *et al.*, 2010, 2012; Sun *et al.*, 2012, 2014; Chen *et al.*, 2013, 2014; J. Xie *et al.*, 2013; Wang *et al.*, 2014; Huang *et al.*, 2015; Li *et al.*, 2017; Riaz *et al.*, 2017). These studies have revealed large-scale seismic velocity and anisotropy structures within the crust and upper mantle that greatly helped understand regional tectonics of the margin. The CEA permanent network, however, was designed for monitoring regional earthquakes, and is too sparse and heterogeneous to be used for high-resolution seismic imaging of fault zones or small-scale crustal and mantle structures, which require a more dense and uniform broadband seismic array.

1. State Key Laboratory of Geodesy and Earth's Dynamics, Innovation Academy for Precision Measurement Science and Technology, Chinese Academy of Sciences, Wuhan, China; 2. Hubei Subsurface Multi-Scale Imaging Key Laboratory, Institute of Geophysics and Geomatics, China University of Geosciences, Wuhan, China; 3. College of Earth and Planetary Sciences, University of Chinese Academy of Sciences, Beijing, China; 4. Department of Earth, Environmental and Planetary Sciences, Rice University, Houston, Texas, U.S.A.

*Corresponding author: zhengyong@cug.edu.cn

Cite this article as Zeng, S., Y. Zheng, F. Niu, and S. Ai (2020). Measurements of Seismometer Orientation of the First Phase CHINArray and Their Implications on Vector-Recording-Based Seismic Studies, *Bull. Seismol. Soc. Am.* **111**, 36–49, doi: [10.1785/0120200129](https://doi.org/10.1785/0120200129)

© Seismological Society of America

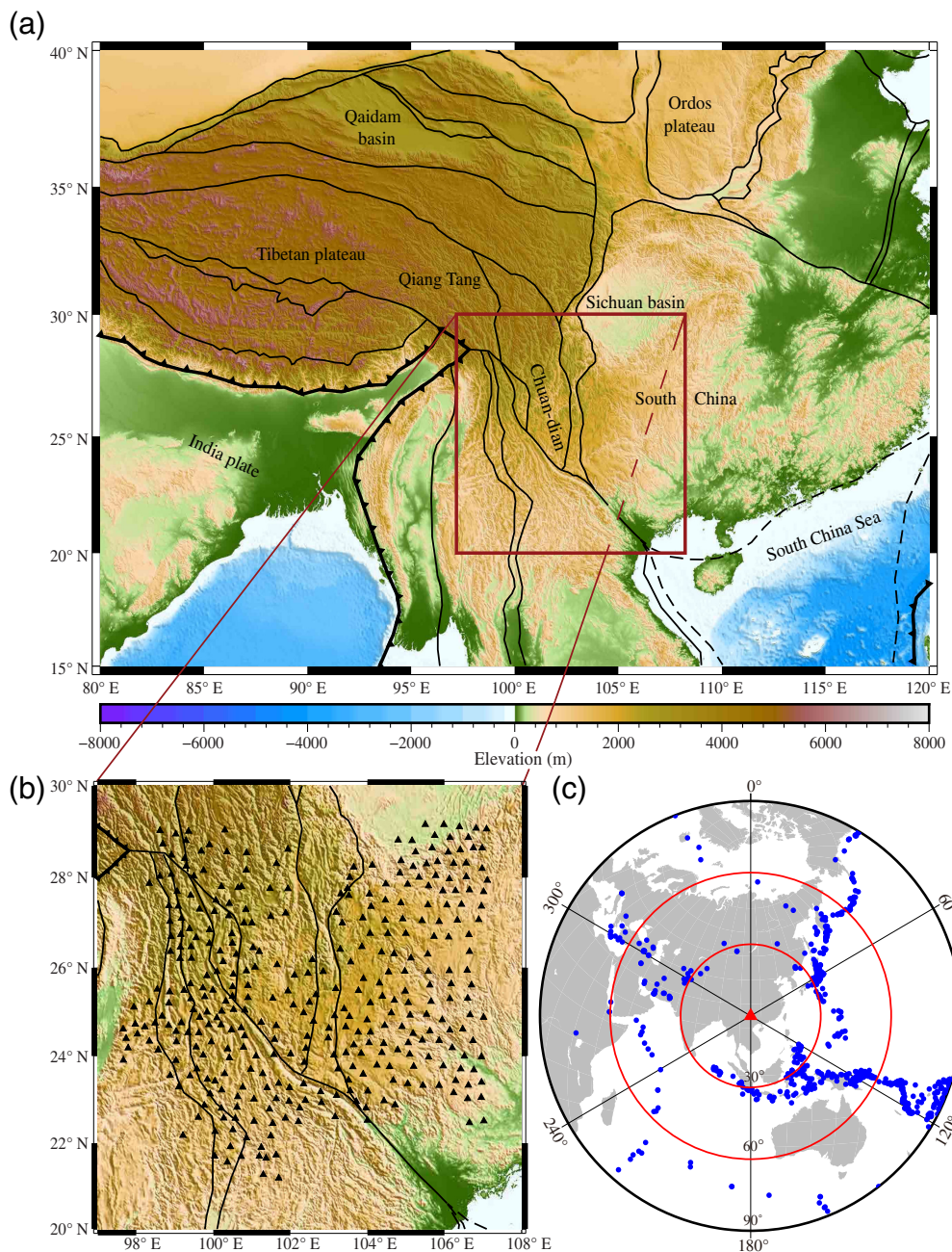


Figure 1. (a) Topographic map showing the Tibetan plateau and its surrounding areas. Black lines indicate boundaries of plates and tectonic blocks. The rectangle indicates the southeastern margin of the Tibetan plateau where the CHINArray phase 1 deployment is located. The margin also marks the southern segment of the south–north earthquake belt in central China. (b) Topographic map showing the 350 CHINArray-I broadband stations (solid triangles) that were deployed between 2011 and 2013. Black lines indicate major faults in the area. (c) Location of the 869 earthquakes (solid circles) used in estimating azimuths of the N -component of all the stations. They were also used in computing receiver functions used in evaluating the misalignment-induced effect on H - κ analysis and crustal anisotropy measurements. The solid triangle at the center of the circles indicates array center, roughly located at 25° N and 105° E. Note that although some events fall into the 30° circle from the array center, all the seismograms that we used have an epicenter distance between 30° and 90° . The color version of this figure is available only in the electronic edition.

The CHINArray project aimed to obtain high-resolution seismic images of the Earth's lithosphere beneath Mainland China to understand lithosphere deformation and to assess

earthquake hazard. The project planned to deploy a dense transportable array (TA) of broadband seismometers across China in multiple phases under the leadership of the Institute of Geophysics, CEA. The phase I deployment started from the southeastern margin of the Tibetan plateau that marks the southern segment of the NSEB. A total of 350 broadband seismographs were deployed with a station spacing of ~ 30 km from 2011 to 2013 (Fig. 1). Hereafter, we refer it to as CHINArray-I.

In general, the orthogonality between components of modern broadband seismographs is highly accurate. Orientation of the three components, however, could deviate from the targeted directions during and after the installation for various reasons. If a compass is used in aligning sensors during a deployment, local anomalies of the magnetic field could lead to a deviation in sensor orientation. During the operation stage, ground subsidence can also cause some changes in sensor alignment. Occasionally, component azimuth might be also altered during service runs, either purposely or unintentionally. Thus, it is of great importance to have an independent estimate of sensor orientation at different periods using their recordings.

Laske (1995) studied the polarity of long-period surface waves recorded at 24 GEOSCOPE stations and 13 International Deployment of Accelerometers (IDA) stations, he found that there were orientation problems at four stations. Schulte-Pelkum *et al.* (2001) analyzed the long-period P waves of the Global Seismic

Network (GSN) recorded between 1976 and 1999 and found there were at least 10 sensors misaligned by more than 10° . Ekström and Busb (2008) showed that $\sim 7.4\%$ of the TA

stations had a misalignment $>7^\circ$, which was confirmed by direct measurement using an interferometric fiberoptic gyroscope. Niu and Li (2011) developed a method to estimate sensor orientation by comparing P -wave particle motions of teleseismic earthquakes and their back azimuths and used it to investigate sensor orientations of the CEArray, which comprises >1000 seismic stations, including 850+ broadband stations operated by the CEA (Zheng *et al.*, 2009). The CEArray stations were aligned by a compass and were installed inside vaults and huts constructed with concrete and steel rebar, which turned out to significantly affect compass measurements. Niu and Li (2011) found a total of 270 CEArray stations that have one or more problems in component azimuth, component nomenclature, and polarity in the initial operation stage.

In general, sensor orientation is determined using either surface waves or body waves under the assumption that horizontal particle motion directions of the P and Rayleigh waves align with their propagation directions, that is, the great circle ray-path directions determined by locations of earthquakes and receivers. Examples of using intermediate- and long-period surface waves to calculate component azimuths have been discussed by Laske and Masters (1996), Larson and Ekström (2002), Ekström and Busb (2008), and Doran and Laske (2017). This method synthesizes seismograms based on earthquake source mechanism and determines component azimuths by minimizing differences between the observed and synthetic data. Zha *et al.* (2013) extended this method to empirical Green's function data computed from ambient noise to determine sensor orientations of ocean bottom seismographs. Because of low signal-to-noise ratio (SNR) of the empirical Green's function data, the method requires a long observational period to obtain robust measurements. Niu and Li (2011) proposed using intermediate-frequency band (0.02–0.2 Hz) P -waveform data of teleseismic earthquakes to determine sensor orientations. Teleseismic P waves generally are of higher frequency than surface waves. In addition, teleseismic P waves are also expected to be less influenced by strong lateral heterogeneities within the lithosphere. Both features suggest that they are ideal sources for constraining sensor orientations.

Multiple institutions were involved in the deployment and operation of CHINArray-I stations; each institution had a slightly different way in installing and servicing its stations. This means that various degrees of misalignment might have existed at different stages of the deployment. The CHINArray-I data have been widely used to map seismic velocity and anisotropy structure of the lithosphere and upper mantle beneath the margin (Sun *et al.*, 2014; Bao *et al.*, 2015; Chang *et al.*, 2015; Cai *et al.*, 2016; Shen *et al.*, 2016; Wang *et al.*, 2017, 2018; Xie *et al.*, 2017; Zhang *et al.*, 2018; Wang and Niu, 2019; Zheng *et al.*, 2019). These studies have improved our understanding of the regional tectonics and seismic hazards. However, we believe that the advantage of the CHINArray-I waveform dataset might not have been fully

explored without knowledge of the orientation of the two horizontal components during the deployment because many seismic imaging techniques rely on the vectorial nature of three-component recording. For example, receiver function technique helps extract P -to- S converted waves through proper rotations of three-component records. During the preprocessing, many waveforms with significant misalignment are generally discarded, which can lead to insufficient stacking and thereby reduce the stability of the results.

In this study, we used the method proposed by Niu and Li (2011) to analyze P -wave polarity of teleseismic records to calculate component azimuths of the 350 CHINArray-I stations. Because the component azimuth of a station might be different in different time periods, we conducted analyses separately for different periods that were obtained by a trial-and-error approach. We then assessed the impact of misalignment to results of three commonly used seismic analyses: H - κ stacking of receiver function data, constraining crustal azimuthal anisotropy with Moho P_s data, and constructing multi-component Green's functions from ambient-noise data. This was done by comparing results from three-component data before and after corrections of misalignment. We found that the differences could be significant when moderate to large deviations in sensor orientation are present.

CHINARRAY-I DATA

As mentioned, the large and dense broadband array we used in this study is the first phase deployment of the CHINArray project that covered the southeastern margin of the Tibetan plateau (Fig. 1a). The temporary array consisted of 350 stations and was deployed between 2011 and 2013 with a station spacing of ~ 30 km (Fig. 1b). Each seismograph is equipped with a Güralp CMG-3ESP or CMG-40T seismometer and a RefTek-130 digitizer with a sampling rate of 100 samples per second. We selected a total of 869 earthquakes that have a moment magnitude >5.5 and are located in the epicenter distance range of 30° – 90° to the CHINArray-I stations. These earthquakes occurred between 2011 and 2013 and are shown in Figure 1c. The number of earthquakes available for most of the 350 stations is >200 . In general, both the back-azimuthal and epicentral distance coverage of the earthquakes are reasonably good (Fig. 1c).

For each station, we first aligned all the seismograms at calculated P -wave arrivals of the iasp91 model (Kennett and Engdahl, 1991). We further applied a two-pole Butterworth band-pass filter of 5–50 s to all the waveform data. We then computed the SNR of the two horizontal components and selected the seismograms that have a summed SNR >5 . Finally, we manually reviewed all the seismograms to ensure that the selected time windows have the proper P -wave arrivals.

METHOD

We adopted the method developed by Niu and Li (2011) to determine sensor orientations by comparing the horizontal

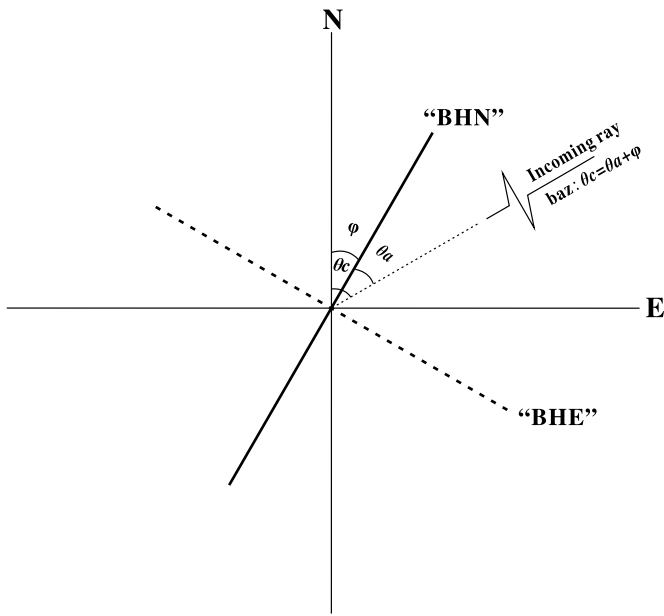


Figure 2. A schematic diagram showing the relationship among the three angles used in the study: azimuth of the BHN component (φ), P -wave particle motion direction (θ_a), and station back azimuth (θ_c). All the angles are defined as positive clockwise.

particle motion directions of teleseismic P waves and the geometric back-azimuth directions of the teleseismic earthquakes. Here, we briefly review the method used in [Niu and Li \(2011\)](#) to measure component azimuth using intermediate-frequency band teleseismic P waves.

SNR-weighted multievent grid search

As shown in the schematic [Figure 2](#), we first assume that the “north” component (BHN or N -component) is misaligned by φ degrees defined clockwise from north. For an incoming teleseismic P wave, θ_c is the true arrival back azimuth. The back azimuth can be computed from the geographic locations of the teleseismic earthquakes and seismic stations using spherical trigonometry. Here, we assume that the Earth can be approximated by a 1D isotropic velocity model such that the P wave propagates through the great circle plane defined by the hypocenter and station. θ_a is the apparent P -wave particle motion direction, which can be computed from the covariance matrix of the two horizontal components (u_N, u_E):

$$c_{ij} = \int_{T_1}^{T_2} u_i(t)u_j(t)dt \quad i, j = N, E, \quad (1)$$

in which T_1 and T_2 mark the beginning and end times of the P -wave arrival. In the absence of noise, we expect the covariance matrix, \mathbf{c} , to have only one nonzero eigenvalue, and θ_a is the direction of the corresponding eigenvector. When noise is present, there are two nonzero eigenvalues, λ_1, λ_2 ($|\lambda_1| \geq |\lambda_2|$), and θ_a corresponds to the direction of the

dominant one (λ_1). The ratio of the two eigenvalues, λ_2/λ_1 , defines the linearity of the particle motion and is an index of noise level and near station scattering that directly affect the error in the measurement of θ_a . Based on the geometry shown in [Figure 2](#), the apparent component azimuth, φ , is the difference between the back azimuth (θ_c) and the particle motion azimuth (θ_a), that is, $\varphi = \theta_c - \theta_a$.

In principle, for each station, we can obtain a misalignment angle, φ , from each single earthquake, and we can take the average of these angles as the azimuth of the N -component of the station. When large noise is present, the individual φ measurements could have very large fluctuations, which could significantly bias the average values. Therefore, [Niu and Li \(2011\)](#) proposed a grid-search method to find the optimum φ that minimizes the summed transverse-component energy of all the events recorded at the stations:

$$E_T(\varphi) = \left(\sum_{i=1}^N w_i E_T^i(\varphi) \right) / \sum_{i=1}^N w_i, \quad (2)$$

in which $E_T^i(\varphi)$ is the transverse-component energy of the i th event, and N is the total number of events; we took the average of the SNR of the two horizontal components as the weights w_i . Before calculation, we used the total P -wave energy recorded on the three components for normalization. We searched φ from 0° to 180° with an increment of 1° . The φ corresponding to the minimum P -wave energy is the best-estimated value. Considering the symmetry of quadrants, the minimum transverse energy value can be obtained when the component azimuth is φ or $\varphi + 180^\circ$. To differentiate the two values, we computed the cross correlation between the vertical and radial components and selected the azimuth corresponding to the positive correlation as the final result.

Error estimation

In an isotropic 1D Earth, we do not expect the transverse component to record any P -wave energy. Thus, E_T^{\min} should follow the χ^2 distribution because it is a sum-of-square Gaussian noise. If there is no P -wave energy on the T -component, then E_T/E_T^{\min} is expected to follow an F -distribution, whose confidence level can be computed by the following equation ([Jenkins and Watts, 1968](#)):

$$\frac{E_T(\varphi)}{E_T^{\min}} \leq 1 + \frac{k}{n-k} f_{k,n-k}(1-\alpha), \quad (3)$$

in which α is the confidence level and n and k are numbers of degree of freedom and parameters. Here, we took $k = 1$, $\alpha = 0.05$, and n as 1 degree of freedom per second ([Silver and Chan, 1991](#)). We also used noise level prior to the P -wave arrival to replace E_T^{\min} in equation (3). For each event, we also used the χ^2 distribution statistics to obtain the upper and lower bounds of misalignment angle φ .

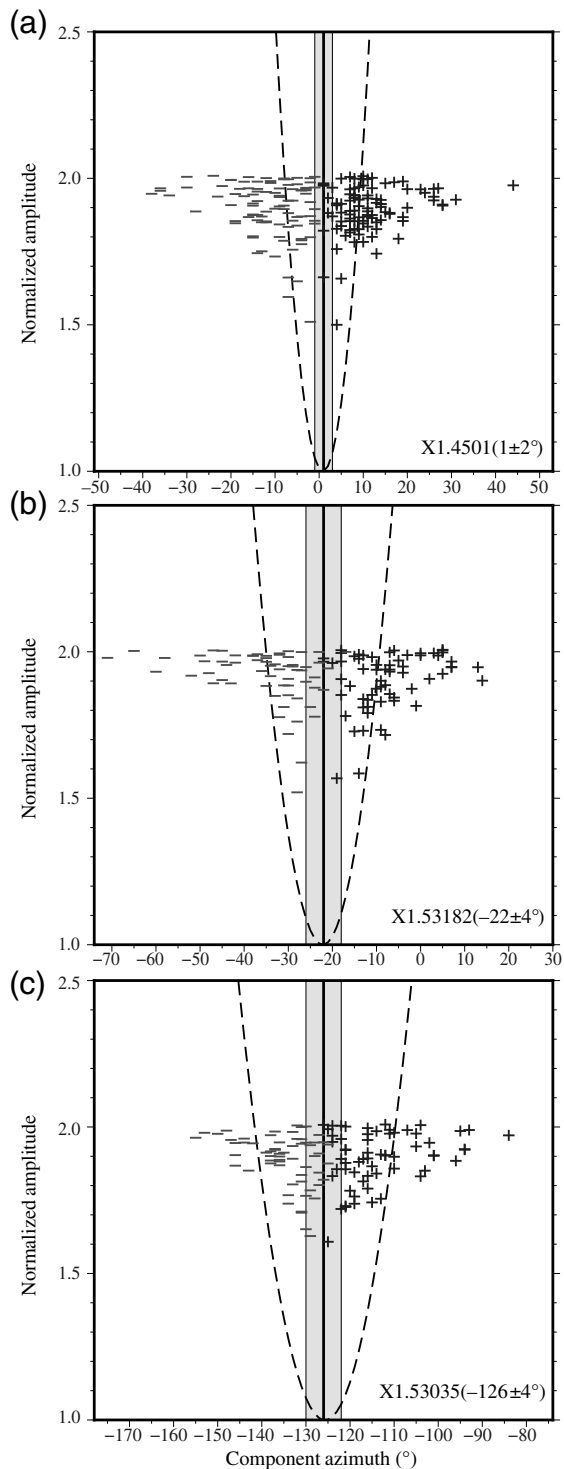


Figure 3. (a) Multievent measurement at station X1.4501. The thick vertical line and the gray area indicate the estimated azimuth, φ , of the N -component and the uncertainty range, respectively, which were derived from the grid search with all the events. Pluses and minuses represent the upper and lower bounds of φ measured from individual earthquakes. The dashed line indicates the summed T -component energy in the P -wave time window, which was normalized by prearrival noise levels. The normalized P -wave energy varies with the assumed azimuth of the N -component and reaches a minimum at 1° . (b) Similar to (a) except for station X1.53182, which has N -component azimuth of $-22^\circ \pm 4^\circ$. (c) Same as (a) except for station X1.53035 with a component azimuth of $-126^\circ \pm 4^\circ$.

Figure 3 shows measurement examples at three stations X1.4501 (Fig. 3a), X1.53182 (Fig. 3b), and X1.53035 (Fig. 3c), which showed a minor ($-2^\circ \pm 2^\circ$), moderate ($-22^\circ \pm 4^\circ$), and significant ($-126^\circ \pm 4^\circ$) misalignment of the N -component, respectively. Here, the normalized energy of the transverse component is shown as a function of assumed sensor orientation. Pluses and minuses are the upper and lower bounds of φ estimated from individual events, and the optimum solution (thick vertical line) falls well between them. As shown in Figure 3, single-event measurement tends to have large uncertainty; Niu and Li (2011) discarded measurements from stations with fewer than five events. Among the 350 stations, only one station, X1.52035, had four events, resulting in a measurement of $-16^\circ \pm 8^\circ$.

We also noticed that the sensor orientation of some stations changed during the deployment, which was likely due to either adjustment during service runs or subsidence of sensor foundation caused by nearby flooding, landslides, and other natural processes. For these stations, when we first ran the grid search with all the events, they generally showed large errors and systematic differences between different periods. So, we divided the deployment into two or more periods and reran the grid search for each period until we obtain a consistent measurement for each period. In addition to the misalignment, we also identified other issues at some of the stations, such as clock errors, frozen components, large deviations in leveling, and so forth, which are discussed in the Results section.

RESULTS

We applied the earlier analysis to all the 350 CHINArray-I stations and obtained misalignment of the N -component from all the stations. Our results suggest that although the deployment of CHINArray-I was very carefully prepared and the uptime of operation was very high, there were still many stations with misalignment angles $>5^\circ$. In addition to misalignment, we found several other issues.

We found that some stations have an issue of polarity reversal. This was identified from comparisons with surrounding stations. More specifically, we first created a subarray by combining each station with its surrounding stations, usually 3–6 stations. We then stacked each component's seismograms of the subarray to create a template for computing cross-correlation coefficients. If the station showed a negative or low cross-correlation coefficient (<0.9), we then manually checked the station and determined whether the station had a reversed polarity.

We also found that the Global Positioning System (GPS) timing of some stations had problems, with the P -wave arrivals being shifted by dozens of seconds. To identify stations with clock errors, we first used the same subarray to confirm whether the P arrival times are consistent. When we found a significant difference (>1 s) from its neighboring stations in P -wave arrival time, we further computed the S -wave arrival

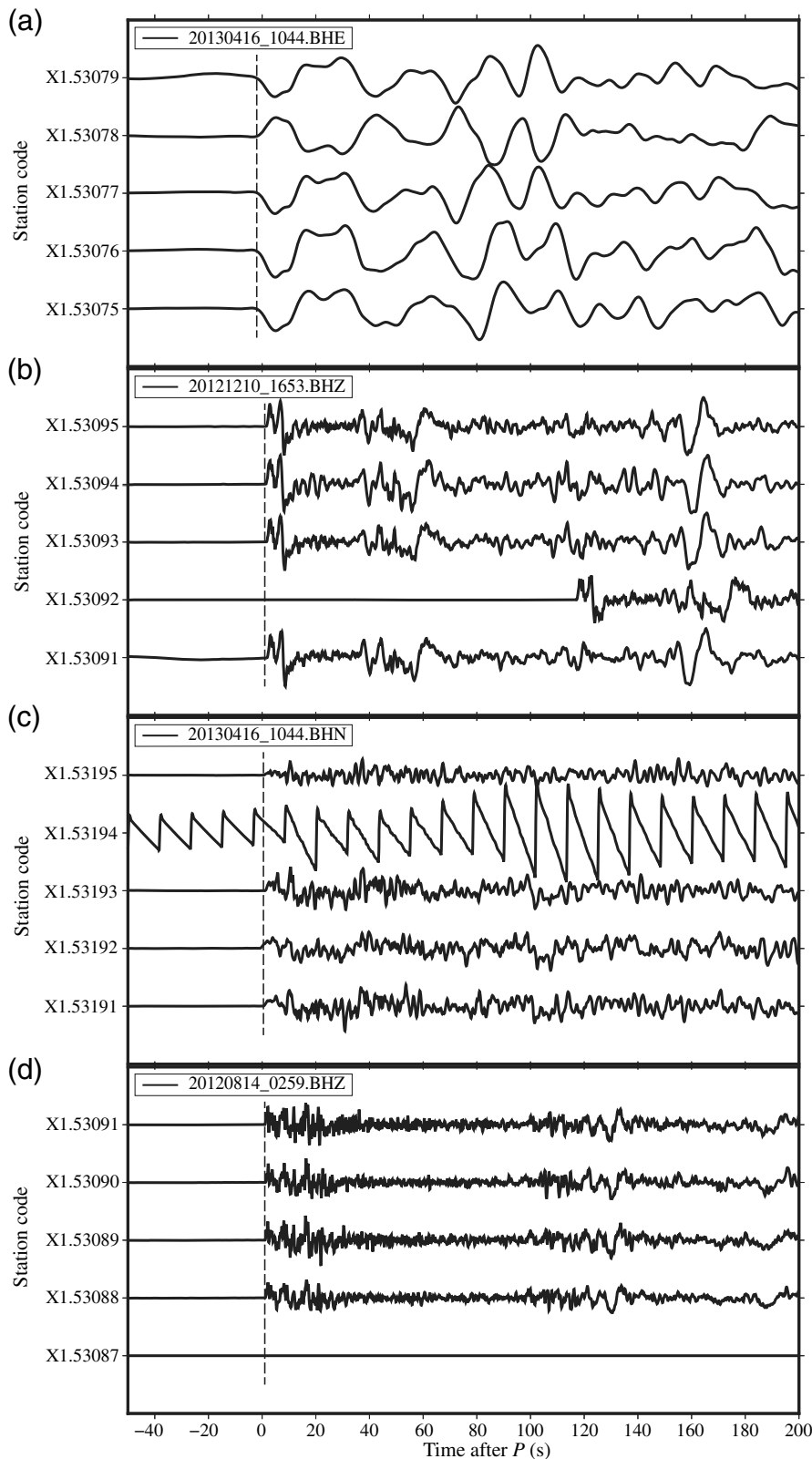


Figure 4. Stations with different types of glitches, aligned with the theoretical P -wave arrival time of the iasp91 model. (a) For station X1.53078, the BHE component is reversed; (b) for station X1.53092, the clock is late by ~ 120 s; (c) for station X1.53194, the BHN component records a distorted waveform; and (d) for station X1.53087, the BHZ component was either locked or dead.

time differences. If the differences of both P and S waves were the same, then we attributed the difference as a clock error. In most cases, we found clock errors were much larger than 1 s, in the order of a few tens to 100 seconds.

The most time-consuming analysis was identifying the stations that had changed their recording properties during the deployment. In some cases, instruments at a station could be adjusted, redeployed to a slightly different location, or replaced by a new seismometer, which could result in different component azimuths in different periods. In this case, if we ran the grid search with the entire event data, we found that the measurement errors were unusually large, and estimates from individual earthquakes jumped from one range to another range at certain time(s). We tried to use times of service visits or data interruption as the breakpoint(s) to divide the deployment into two or more periods and then ran the grid search of misalignment angle separately for each period. If the measured values of φ from different periods were similar, which were close to the result obtained from the entire earthquake data, then we assumed that no physical changes were made to the stations during the service runs, and the results obtained from all events were taken as the final results. Otherwise, we kept the azimuthal deviation results of different time periods.

Figure 4 shows four types of instrumental glitches that we found. Here, we aligned the data with the theoretical P -wave arrival time calculated

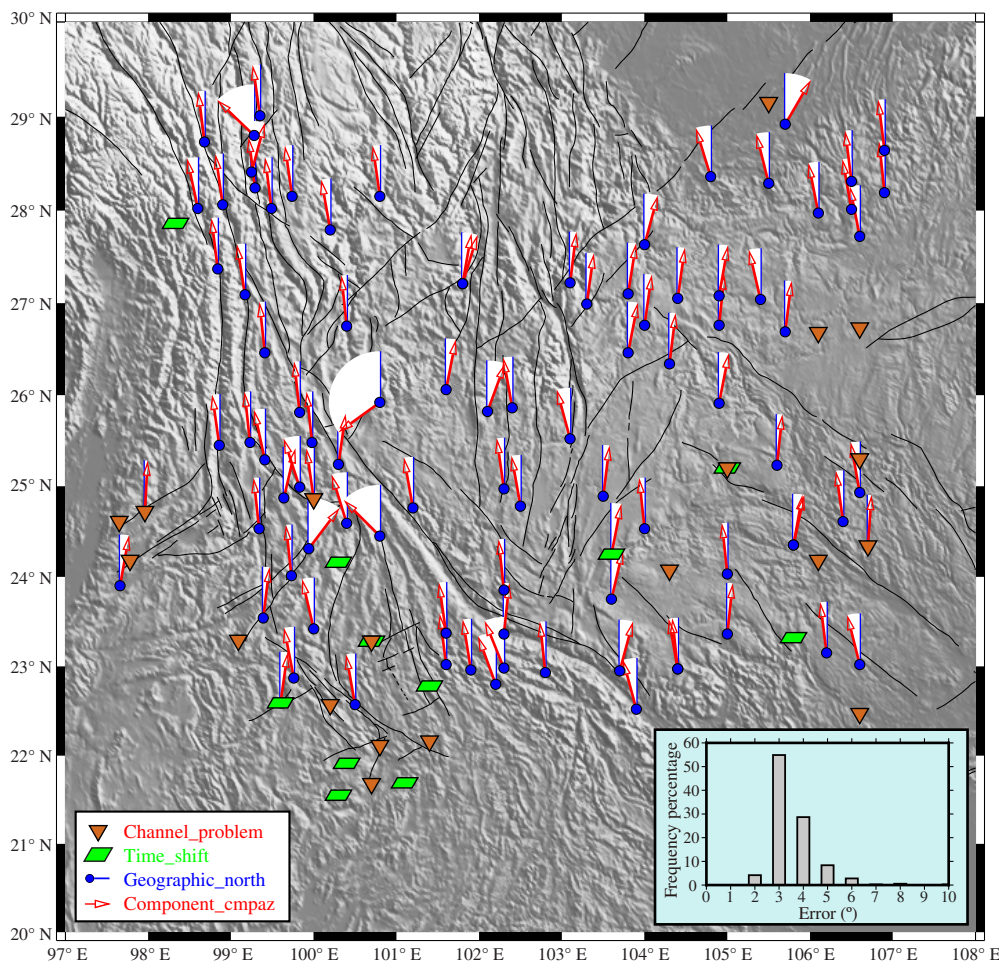


Figure 5. Map shows the 129 stations with a misalignment angle $>5^\circ$ and other malfunctions. Parallelograms indicate stations with a drifted clock, and inverted triangles represent stations with at least one component that had some glitches over part of or entire period of the deployment. Solid circles indicate stations with a $5^\circ + N$ -component azimuth being indicated by the open arrows. Inset shows the histogram of measurement uncertainty of all 350 stations. The color version of this figure is available only in the electronic edition.

with the iasp91 model. In Figure 4a, it can be clearly seen that the P waveform recorded at the station X1.53078 had an opposite polarity than those of the neighboring stations. In other words, the north component of instrument was actually pointing to south by mistake. Figure 4b shows the waveforms of station X1.53092 had a clock error of ~ 120 s. These mistakes might be related to the GPS timing system. The N -component of station X1.53194 shown in Figure 4c seemed to have periodic interference or failures, which may be caused by unstable voltage or environmental disturbance, resulting in uncorrectable and therefore unusable waveforms. A more serious situation was shown in Figure 4d, with the amplitude of the Z -component of station X1.53087 being close to 0, suggesting that this component was likely either locked or damaged. If these types of invalid records had been used in computing ambient-noise cross-correlation functions (CCFs), the problem might not be easily recognized because the data

preprocessing normalized the continuous records with either one-bit representation (Shapiro *et al.*, 2005), spectral whitening (Bensen *et al.*, 2007), or other algorithms.

The estimated misalignment angles (φ) of the CHINArray-I stations are shown in Figure 5. Among the 350 stations, 220 stations have an N -component orientation deviation $<5^\circ$, 80 stations have a misalignment angle between 5° and 20° , and 49 stations have a misorientation $>20^\circ$ or other failures. Supplemental material to this article lists the misalignment angles of the 129 problematic stations, together with the measurement uncertainties and the number of earthquakes used in the analyses.

DISCUSSION

In our measurements of particle motion direction θ_a , we used a fixed 12 s time window ($T_1 = -2$ s, $T_2 = 10$ s) in computing the covariance matrix defined in equation (1). We also tried other fixed length time windows, such as ($T_1 = -2$ s, $T_2 = 8$ s) and ($T_1 = -2$ s, $T_2 = 12$ s), and

we found that the results were almost the same. We also hand-picked the beginning and end time of the P waves from all the earthquakes at two stations and used them in computing the covariance matrices. The estimated misalignment angles were also very similar to the 12 s window measurements. Thus, we concluded that P -wave time-window selection had little influence on our measurements.

We have assumed that P -wave particle motion directions are parallel to their propagation directions based on a first-order approximation of the Earth with a 1D isotropic medium. In addition to sensor misalignment and noise, deviations of P -wave particle motion direction can be caused by lateral heterogeneities, seismic anisotropy, and dipping boundaries within the 3D Earth (Niu and Li, 2011). These 3D structures are expected to result in different systematic variations with respect to the incoming P -wave direction (Schulte-Pelkum *et al.*, 2001; Davis, 2003; Fontaine *et al.*, 2009). Davis (2003)

found that deviations induced by mantle seismic anisotropy are rather trivial, usually $<1^\circ$, based on numerical simulations. Schulte-Pelkum *et al.* (2001) found that the 264 stations of the GSN had a median deviation of 7.2° in P -wave particle motion. Niu and Li (2011) attributed this deviation to be caused jointly by sensor misorientation, noise, and 3D subsurface structures and used a deviation of 8° as the threshold to determine whether a sensor has an issue of misalignment. Here, we used a slightly different value to categorize sensor misorientation. The inset in Figure 5 shows the histogram of the measurement errors, which are distributed in the range of 1° – 10° with a peak of 3° . More than 95% of the error estimates are $<5^\circ$, which led us to categorize stations with a deviation angle $<5^\circ$ as normal orientation or minor misalignment. We further labeled sensors with a deviation angle of 5° – 20° as moderately misaligned stations and those above 20° as severely or significantly misaligned stations.

As stated before, modern seismic studies rely on three-component seismic recordings being properly aligned. In the rest of this section, we discussed how sensor misalignment adversely affects three commonly used seismic analyses, H - κ stacking of receiver function data, estimating crustal azimuthal anisotropy with Moho P_s converted wave, and extracting Rayleigh-wave Green's functions from multicomponent ambient-noise data. Our approach is quite straightforward: we selected four stations that have significant misalignments—X1.53182 ($\varphi = -22^\circ$), X1.51046 ($\varphi = -46^\circ$), X1.53035 ($\varphi = -126^\circ$), and X1.4510 ($\varphi = 180^\circ$)—and then conducted the three types of analyses using the original and corrected waveform data. The two sets of results were finally contrasted to illustrate the adverse effects of sensor misalignment.

Influence on H - κ stacking

The H - κ stacking technique was proposed by Zhu and Kanamori (2000) to use Moho P_s conversion and crustal multiples recorded by receiver functions to constrain crustal thickness (H) and the average V_p/V_s ratio (κ) of the crust. For the previous four stations, we manually selected waveform data with high SNR from the same teleseismic dataset used in determining orientation of the N -component. We then rotated the two horizontal components to the radial and transverse directions based on default and measured component azimuths. We then created two sets of receiver functions by deconvolving the vertical component from the two sets of radial-component data. We used the improved H - κ stacking method proposed by Niu *et al.* (2007), which introduced a cross-correlation-based weighting function in summing the Moho P_s conversion ($0p1s$) and the two multiples ($2p1s$ and $1p2s$). Here, we used the nomenclature of Niu and James (2002) to refer to these receiver function phases. The notation, $npms$, indicates n P -wave legs and m S -wave legs traveling inside the crust beneath the station. We used P -wave velocity of CRUST 1.0 (Laske *et al.*, 2013) and set a weighting scheme of 0.5, 0.25, and 0.25 for the

three phases, $0p1s$, $2p1s$, and $1p2s$ in grid searching the best combination of (H , κ).

The H - κ stacking results of the four stations are shown in Figure 6, with the left and right columns showing the results from receiver functions generated from data before and after the correction of sensor misorientation. The (H , κ) values measured at station X1.53182 with a misalignment of -22° from uncorrected and corrected receiver functions are almost the same, except that the results of corrected data showed a better convergence and smaller errors (Fig. 6a,b). In the case of station X1.51046 with a misorientation of -46° , the search results showed a difference of 2 km in crustal thickness in addition to the difference in convergence (Fig. 6c,d). For this station, we reduced the search range of the (H , κ) to decrease trade-off-induced ambiguities. For the third station, X1.53035, which has an N -component azimuth of -126° , the H - κ result with the original receiver functions was very unstable, meaning that randomly chosen subsets of receiver functions yielded very different results (Fig. 6e,f). The H - κ search using receiver functions created with the measured φ , on the other hand, converges well to a crustal thickness of ~ 50 km, which is consistent to the measurements of nearby permanent stations (Sun *et al.*, 2012). We observed a similar discrepancy at station X1.4510, where the two horizontal components were aligned in the opposite directions, that is, $\varphi = 180^\circ$ (Fig. 6g,h). After correcting the misalignment, we obtained a crustal thickness of ~ 30 km beneath the station, which is also similar to the results of its neighboring stations as well as nearby permanent stations (Sun *et al.*, 2012). From our simple experiment, we concluded that a moderate misalignment of N -component by 20° appears to have little to no effect on the estimated values of (H , κ) but with larger measurement uncertainties. When the degree of misalignment increases, then the H - κ searching using uncorrected data becomes unstable and leads to incorrect estimates of both crustal thickness and V_p/V_s ratio.

Influence on measurement of crustal seismic anisotropy

Seismic anisotropy is the directional dependence of propagation speed of seismic waves. In an anisotropic medium, seismic waves travel at different velocities depending on their propagation and polarization directions. Seismic anisotropy is believed to be related to aligned crystal and other structures within the crust and upper mantle and thereby has been used to infer the past or present dynamic processes that have led to the alignments (Savage, 1999). Studies of seismic anisotropy generally require three-component data, and the fast polarization direction is a physical quantity that is directly correlated to the component azimuth.

Here, we evaluate how sensor misorientation affects measurement of crustal azimuthal anisotropy using the Moho P_s conversion waves recorded by receiver functions. We used the technique developed by Liu and Niu (2012) that determines

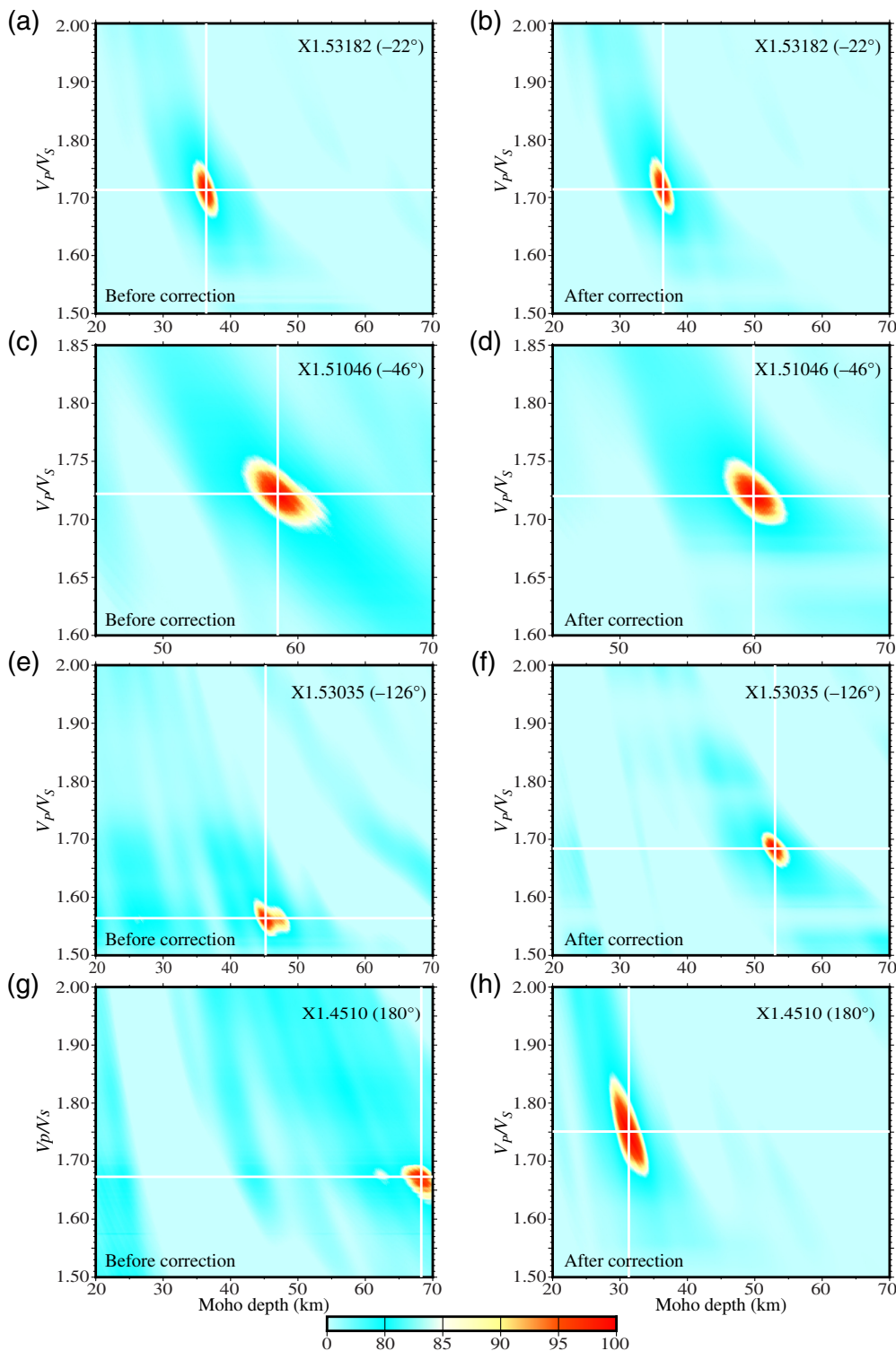


Figure 6. Comparison of H - κ grid-search results using receiver functions recorded at stations with moderate to severe misalignments of the two horizontal components, which were ignored (left) or taken into account (right). Contour of the weighted summed amplitude of the $0p1s$, $2p1s$, and $1p2s$ is shown as a function of crustal thickness (horizontal) and V_p/V_s ratio (vertical). Location of the amplitude peak is indicated by the two white lines. (a,b) Results of station X1.53182 with a misalignment of -22° . The measurement difference in crustal thickness is <1 km. (c,d) Results at station X1.51046 with an N -component azimuth of -46° . The estimated crustal thickness has a difference of ~ 2 km. (e,f) Results at station X1.53035 with a large misorientation $\varphi = -126^\circ$, the difference in measured crustal thickness is nearly 10 km, and the V_p/V_s ratio is low compared with nearby stations before correction. (g,h) Results at station X1.4510 with two components being completely reversed ($\varphi = 180^\circ$); both the measured crustal thickness and V_p/V_s ratio are very different. The color version of this figure is available only in the electronic edition.

crustal seismic anisotropy by a joint analysis of radial (R) and transverse (T) receiver function. Again, we generated two sets of R and T receiver functions using the default and measured N -component azimuths in coordinate rotation. Readers are referred to Liu and Niu (2012) for more details on the joint analysis method.

To obtain robust estimates of crustal anisotropy, Liu and Niu (2012) proposed computing three individual objective functions (IOFs) and one joint objective function (JOF). The three IOFs were designed to grid search a fast direction (θ) and delay time (δt) between the fast and slow P_s arrivals that (1) maximize the peak energy of the stacked R receiver function after the correction of seismic anisotropy (I_{ra}); (2) maximize the cross correlation of the anisotropy-corrected R receiver functions (I_{rcc}); and (3) minimize the total energy of the anisotropy-removed T receiver function (I_{te}). The three IOFs were further integrated to one JOF (I_{JOF}). We searched the fast direction, θ , in the full azimuthal range of 0° – 360° with an increment of 1° , and the delay time, δt , from 0.0 to 1.5 s with steps of 0.02 s.

We applied the joint analysis on two misaligned stations, X1.53182 and X1.53035, which exhibited a misorientation of -22° and -126° , respectively; the results are shown in Figure 7. The top two panels of Figure 7 show the results of X1.53182 before (Fig. 7a) and after (Fig. 7b) correction of sensor misalignment. In general, the two sets of results are quite similar to each other. However, the estimated

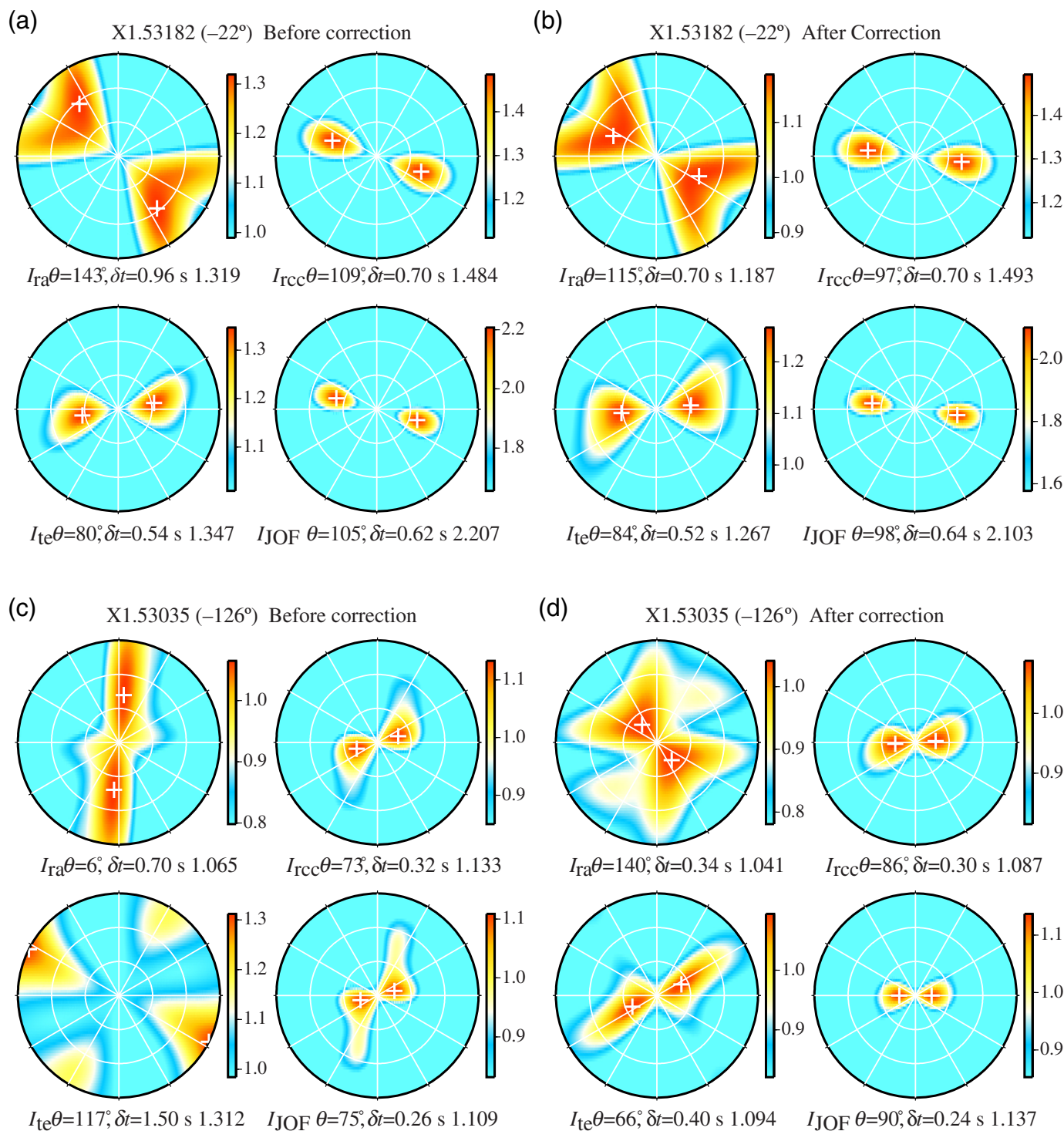


Figure 7. Estimates of crustal anisotropy using R and T receiver functions generated with default and measured azimuths of the two horizontal components are shown in (a,c) and (b,d) for comparison. For each set of measurements, the top two polar plots are results from the individual objective functions (IOFs) using R receiver functions, and the lower-left corner is the result from the third IOF with T receiver functions. The joint objective function (JOF) result is shown at the lower-right corner. (a) Results

of station X1.53182 with no correction of the misalignment of -22° . (b) Results of station X1.53182 after the -22° misalignment being taken into account. (c) and (d) are the same as (a) and (b), respectively, except for the station X1.53035, where the two horizontal components were deviated by as much as -126° . In general, the individual and joint measurements agree with each other in the right panel more than they do in the left panel. The color version of this figure is available only in the electronic edition.

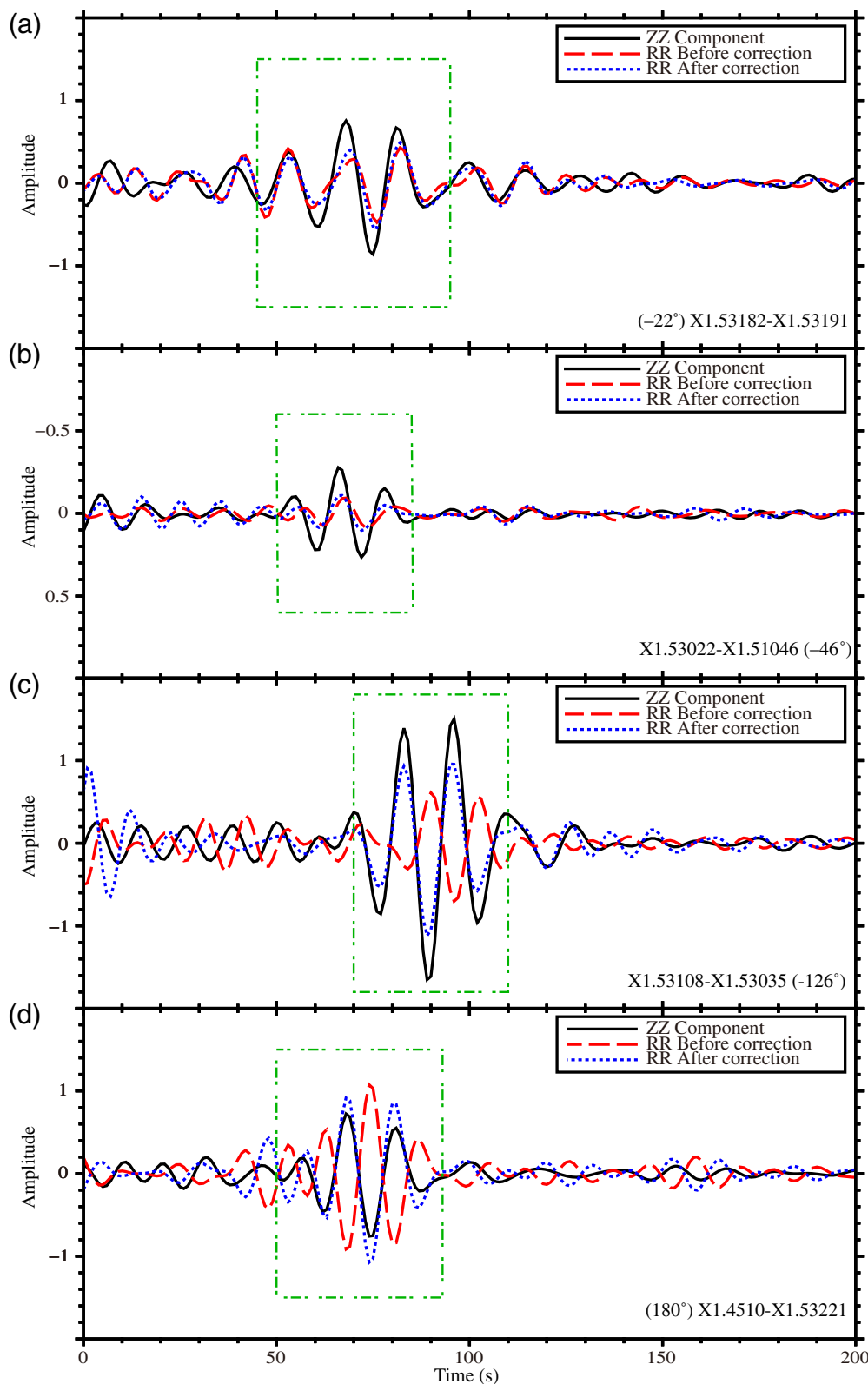


Figure 8. Cross-correlation functions of the ZZ, the default RR, and the corrected RR are shown in solid, dashed, and dotted lines, respectively, for comparison. (a) Station pair X1.53182 ($\varphi = -22^\circ$) and X1.53191. (b) Station pair of X1.51046 ($\varphi = -46^\circ$) and X1.53022. (c) Station pair of X1.53035 ($\varphi = -126^\circ$) and X1.53108. (d) Station pair of X1.4510 ($\varphi = 180^\circ$) and X1.53221. All the second stations in each pair had a normal north-south/east-west component orientation. Note that the dotted lines (corrected RR) are generally in phase with the solid lines (ZZ), and the dashed lines (uncorrected RR) are lagged by $\sim 1/10$ to 1π , which is proportional to the amount of misalignment of the two horizontal components. The color version of this figure is available only in the electronic edition.

anisotropic parameters from the three IOFs appeared to be more consistent with each other after the correction of misorientation, indicating that moderate sensor misalignment has an adverse effect on the stability of the individual grid searches. Results of the more severely misoriented station, X1.53035, are shown at the bottom two panels of Figure 7. The fast polarization direction and delay time obtained before and after correction of sensor azimuth are shown in the left (Fig. 7c) and right (Fig. 7d), respectively. Here, the differences between the two sets of measurements are obvious, and the results with the corrected receiver function data are evidently more stable, especially the estimate from the T receiver functions shown in the lower-left corner of each panel.

Influence on computing Rayleigh-wave Green's function from ambient-noise data

The ambient-noise field can be largely approximated by a diffuse field, and the Green's function between two seismic stations can be obtained from the cross correlation of the field (e.g., Lobkis and Weaver, 2001; Shapiro *et al.*, 2005). Early usage of ambient noise focuses mainly on phase or group velocity extraction from Rayleigh-wave Green's functions between two stations that were computed from cross correlating the vertical-component recordings of the two stations. Recently, CCFs of three-component recordings have been computed to constrain other properties of surface waves, such as the Rayleigh-wave ellipticity, or

the vertical and horizontal amplitude ratio of the Rayleigh wave, known as the Z/H ratio, which appears to provide better constraints on shallow structures than phase or group velocities do (Chong *et al.*, 2014; Li *et al.*, 2016). The three-component CCFs are commonly referred to as cross-correlation tensor (CCT).

To evaluate how sensor misalignment affects the extraction of CCTs, we again used the aforementioned four stations, X1.53182, X1.51046, X1.53035, and X1.4510, which had measured N -component azimuths of -22° , -46° , -122° , and 180° , respectively. We collected 1 yr (2012) continuous data of the four stations and another four nearby stations. We followed Li *et al.* (2016) to compute the daily CCTs of the four station pairs, which were further stacked to obtain the final CCTs. Data preprocessing was largely based on Bensen *et al.* (2007), which includes removal of instrument response and linear trends, temporal whitening of daily continuous records, and so forth. We then rotated the elements of final CCTs to the ZZ and RR CCFs and further filtered the CCFs with a 0.05–0.1 Hz Butterworth band-pass filter.

Because we applied the component-azimuth correction only to the two horizontal components, we have two sets of RR CCFs, one before and one after the correction, and one set of ZZ CCF that requires no correction, for comparison. In theory, the ZZ and RR CCFs are expected to have the same phase, that is, they align in phase. The computed ZZ and two RR CCFs of the four stations and their pairing stations are plotted in solid, dashed, and dotted lines in Figure 8, respectively, in the order of X1.53182 (Fig. 8a), X1.51046 (Fig. 8b), X1.53035 (Fig. 8c), and X1.4510 (Fig. 8d) from the top to the bottom. In general, there is a phase shift between the two sets of RR CCFs. The RR CCFs after proper correction of component azimuth (dotted lines) align more closely with the ZZ CCFs (solid lines). This suggests that a proper correction of misalignment is required to obtain accurate RR CCFs, as well as the more general CCTs. The phase lag of the uncorrected RR CCFs (dashed lines) observed at station X1.53182 shown in Figure 8a with a misalignment of -22° is actually already obvious. This phase lag evidently increases with the degree of misalignment shown progressively in Figure 8b–d. At station X1.53035 (Fig. 8c), where the sensor misorientation reaches to -126° , the phase lag of the uncorrected RR CCF (dashed line) is $>\pi/2$. At the station X1.4510 with a 180° misorientation, the two RR CCFs (dashed and dotted lines) have a polarity reversal, indicating that the RR CCF (dashed line) has a phase lag of π if no correction was made before the calculation.

From the earlier analyses, we concluded that when large sensor misalignments are presented in three-component seismic data acquisition, they could have a large influence on the calculation of receiver functions and ambient-noise CCF tensors. Although we have only investigated the impacts on the previous three particular cases, it is foreseeable that as long

as horizontal-component rotation is involved in an analysis, the component azimuth deviation would have certain adverse effects. Therefore, it is essential to verify component azimuth for any three-component seismic acquisitions. Meanwhile, we hope that the measured N -component azimuths here could benefit future studies that use the CHINArray-I data.

CONCLUSIONS

We conducted an extensive investigation of sensor misorientation of the CHINArray-I deployment using teleseismic P -waveform data. Among the 350 three-component stations, about two-thirds of seismometers (220) were properly aligned during the 2 yr deployment. About 80 seismometers were, however, obviously misoriented by 5° – 20° , and another 49 stations were misaligned by $>20^\circ$ or had some severe glitches during the entire or part of the deployment. We further investigated how misalignment affects three commonly used seismic analyses based on three-component waveform data. Our analyses suggested that when significant misalignments in three-component data were present but were not taken into account, the computed receiver functions could result in unstable and incorrect estimates of crustal thickness, V_P/V_S ratio, and crustal seismic anisotropy. Also, we found the same adverse effect in ambient-noise analysis using misaligned three-component data without a correction of component direction. The elements in the CCF tensor computed from the horizontal components, such as the RR CCFs, were significantly lagged in phase compared with the ZZ element, resulting in incorrect measurements of phase and group velocities, as well as Z/H ratio. However, if the misalignment was taken into account and corrected, then those data from stations with misoriented seismometers could be used to produce results that are as robust and accurate as those from properly aligned recordings.

DATA AND RESOURCES

The waveform data were provided by China Earthquake Administration (CEA) Data Management Center. Details on the permission and rules of using the CHINArray waveform data can be found from the following website (<http://www.cea-igp.ac.cn/kejichuangxinzhuanli/guojiashuzicezhentaiwangshujubeifenzhongxin/index.html>, last accessed June 2020). The earthquake catalog was downloaded from the U.S. Geological Survey (USGS) website (<https://earthquake.usgs.gov/earthquakes/search>, last accessed June 2020). All the figures were prepared using Generic Mapping Tools (GMT; Wessel and Smith, 1998). The supplemental material is the result of the misalignment angles and malfunctioning issues of the 129 problematic stations.

ACKNOWLEDGMENTS

The authors thank the China Earthquake Administration (CEA) Data Management Center for providing the waveform data and Yashan Feng for helping them edit their original manuscript. The authors also thank Associate Editor Eric Chael and two anonymous reviewers for providing very careful and constructive reviews that improved the article

significantly. This work was supported by the Sichuan-Yunnan National Seismic Experiment Field Project (2019CSES0109), the National Natural Science Foundation of China (41874053, 41731072, and 41574057), the State Key Laboratory of Geological Processes and Mineral Resources (Number MSFGPMR01-4), the National Key R&D Program of China (2017YFC1500303), the Yangtze River Project of the University of Geosciences (CUGCJ1707), and the China University of Geosciences (Wuhan) Central Basic Research Fund (162301132637). The corresponding author of this article is Yong Zheng from China University of Geosciences, Wuhan. All of the figures are made with Generic Mapping Tools (GMT) software.

REFERENCES

- Bai, D., M. J. Unsworth, M. A. Meju, X. Ma, J. Teng, X. Kong, Y. Sun, J. Sun, L. Wang, C. Jiang, *et al.* (2010). Crustal deformation of the eastern Tibetan plateau revealed by magnetotelluric imaging, *Nature Geosci.* **3**, 358–362, doi: [10.1038/NGEO830](https://doi.org/10.1038/NGEO830).
- Bao, X., X. Sun, M. Xu, D. W. Eaton, X. Song, L. Wang, Z. Ding, N. Mi, H. Li, D. You, *et al.* (2015). Two crustal low-velocity channels beneath SE Tibet revealed by joint inversion of Rayleigh wave dispersion and receiver functions, *Earth Planet. Sci. Lett.* **415**, 16–24, doi: [10.1016/j.epsl.2015.01.020](https://doi.org/10.1016/j.epsl.2015.01.020).
- Bensen, G. D., M. H. Ritzwoller, M. P. Barmin, A. L. Levshin, F. Lin, M. P. Moschetti, N. M. Shapiro, and Y. Yang (2007). Processing seismic ambient noise data to obtain reliable broad-band surface wave dispersion measurements, *Geophys. J. Int.* **169**, 1239–1260, doi: [10.1111/j.1365-246X.2007.03374.x](https://doi.org/10.1111/j.1365-246X.2007.03374.x).
- Cai, Y., J. Wu, L. Fang, W. Wang, and S. Yi (2016). Crustal anisotropy and deformation of the southeastern margin of the Tibetan plateau revealed by *Pms* splitting, *J. Asian Earth Sci.* **121**, 120–126, doi: [10.1016/j.jseae.2016.02.005](https://doi.org/10.1016/j.jseae.2016.02.005).
- Chang, L., Z. Ding, and C. Wang (2015). Upper mantle anisotropy beneath the southern segment of North-South tectonic belt, China, *Chin. J. Geophys.* **58**, 4052–4067, doi: [10.6038/cjg20151114](https://doi.org/10.6038/cjg20151114) (in Chinese with English abstract).
- Chen, M., H. Huang, H. Yao, R. D. van der Hilst, and F. Niu (2014). Low wave speed zones in the crust beneath SE Tibet revealed by ambient noise adjoint tomography, *Geophys. Res. Lett.* **41**, 334–340, doi: [10.1002/2013GL058476](https://doi.org/10.1002/2013GL058476).
- Chen, Y., Z. Zhang, C. Sun, and J. Badal (2013). Crustal anisotropy from Moho converted *Ps* wave splitting analysis and geodynamic implications beneath the eastern margin of Tibet and surrounding regions, *Gondwana Res.* **24**, 946–957, doi: [10.1016/j.gr.2012.04.003](https://doi.org/10.1016/j.gr.2012.04.003).
- Chong, J., S. Ni, and L. Zhao (2014). Joint inversion of crustal structure with the Rayleigh wave phase velocity dispersion and the ZH ratio, *Pure Appl. Geophys.* **172**, no. 10, 2585–2600, doi: [10.1007/s00024-014-0902-z](https://doi.org/10.1007/s00024-014-0902-z).
- Davis, P. M. (2003). Azimuthal variation in seismic anisotropy of the southern California uppermost mantle, *J. Geophys. Res.* **108**, no. B1, 2052, doi: [10.1029/2001jb000637](https://doi.org/10.1029/2001jb000637).
- Doran, A. K., and G. Laske (2017). Ocean-bottom seismometer instrument orientations via automated rayleigh-wave arrival-angle measurements, *Bull. Seismol. Soc. Am.* **107**, no. 2, 691–708, doi: [10.1785/0120160165](https://doi.org/10.1785/0120160165).
- Ekström, G., and R. W. Busb (2008). Measurements of seismometer orientation at USArray transportable array and backbone stations, *Seismol. Res. Lett.* **79**, no. 4, 554–561, doi: [10.1785/gssrl.79.4.554](https://doi.org/10.1785/gssrl.79.4.554).
- Fontaine, F. R., G. Barruol, B. L. N. Kennett, G. H. R. Bokelmann, and D. Reymond (2009). Upper mantle anisotropy beneath Australia and Tahiti from *P* wave polarization: Implications for real-time earthquake location, *J. Geophys. Res.* **114**, no. B03306, doi: [10.1029/2008jb005709](https://doi.org/10.1029/2008jb005709).
- Huang, Z., P. Wang, M. Xu, L. Wang, Z. Ding, Y. Wu, M. Xu, N. Mi, D. You, and H. Li (2015). Mantle structure and dynamics beneath SE Tibet revealed by new seismic images, *Earth Planet. Sci. Lett.* **411**, 100–111, doi: [10.1016/j.epsl.2014.11.040](https://doi.org/10.1016/j.epsl.2014.11.040).
- Jenkins, G. M., and D. G. Watts (1968). *Spectra Analysis and Its Applications*, Holden-Day, San Francisco, California, 525 pp.
- Kennett, B. L. N., and E. R. Engdahl (1991). Traveltimes for global earthquake location and phase identification, *Geophys. J. Int.* **105**, 429–465, doi: [10.1111/j.1365-246X.1991.tb06724.x](https://doi.org/10.1111/j.1365-246X.1991.tb06724.x).
- Larson, E. W. F., and G. Ekström (2002). Determining surface wave arrival angle anomalies, *J. Geophys. Res.* **107**, no. B6, doi: [10.1029/2000JB000048](https://doi.org/10.1029/2000JB000048).
- Laske, G. (1995). Global observation of off-great-circle propagation of long-period surface waves, *Geophys. J. Int.* **123**, 245–259, doi: [10.1111/j.1365-246X.1995.tb06673.x](https://doi.org/10.1111/j.1365-246X.1995.tb06673.x).
- Laske, G., and G. Masters (1996). Constraints on global phase velocity maps from long-period polarization data, *J. Geophys. Res.* **101**, no. B7, 16,059–16,075, doi: [10.1029/96jb00526](https://doi.org/10.1029/96jb00526).
- Laske, G., G. Masters, Z. Ma, and M. Pasyanos (2013). Update on CRUST1.0—A 1-degree global model of Earth's crust, *Geophys. Res. Abstr.* **15**, 2658, doi: [10.6092/1970-9870/128](https://doi.org/10.6092/1970-9870/128).
- Li, G., H. Chen, F. Niu, Z. Guo, Y. Yang, and J. Xie (2016). Measurement of Rayleigh wave ellipticity and its application to the joint inversion of high-resolution *S* wave velocity structure beneath northeast China, *J. Geophys. Res.* **121**, 864–880, doi: [10.1002/2015JB012459](https://doi.org/10.1002/2015JB012459).
- Li, J., X. Song, L. Zhu, and Y. Deng (2017). Joint inversion of surface wave dispersions and receiver functions with *P* velocity constraints: Application to Southeastern Tibet, *J. Geophys. Res.* **122**, 7291–7310, doi: [10.1002/2017JB014135](https://doi.org/10.1002/2017JB014135).
- Liu, H., and F. Niu (2012). Estimating crustal seismic anisotropy with a joint analysis of radial and transverse receiver function data, *Geophys. J. Int.* **188**, 144–164, doi: [10.1111/j.1365-246X.2011.05249.x](https://doi.org/10.1111/j.1365-246X.2011.05249.x).
- Liu, M., and Y. Yang (2003). Extensional collapse of the Tibetan Plateau: Results of three-dimensional finite element modeling, *J. Geophys. Res.* **108**, no. B8, 2361, doi: [10.1029/2002JB002248](https://doi.org/10.1029/2002JB002248).
- Lobkis, O. I., and R. L. Weaver (2001). On the emergence of the Green's function in the correlations of a diffuse field, *J. Acoust. Soc. Am.* **110**, no. 6, 3011–3017, doi: [10.1121/1.1417528](https://doi.org/10.1121/1.1417528).
- Niu, F., and D. E. James (2002). Fine structure of the lowermost crust beneath the Kaapvaal craton and its implications for crustal formation and evolution, *Earth Planet. Sci. Lett.* **200**, 121–130, doi: [10.1016/S0012-821X\(02\)00584-8](https://doi.org/10.1016/S0012-821X(02)00584-8).
- Niu, F., and J. Li (2011). Component azimuths of the CEArray stations estimated from *P*-wave particle motion, *Earthq. Sci.* **24**, 3–13, doi: [10.1007/s11589-011-0764-8](https://doi.org/10.1007/s11589-011-0764-8).
- Niu, F., T. Bravo, G. Pavlis, F. Vernon, H. Rendon, M. Bezada, and A. Levander (2007). Receiver function study of the crustal structure of the southeastern Caribbean plate boundary and Venezuela, *J. Geophys. Res.* **112**, no. B11308, doi: [10.1029/2006JB004802](https://doi.org/10.1029/2006JB004802).

- Riaz, M. S., Y. Zheng, X. Xiong, Z. Xie, Z. Li, and M. Song (2017). Refined 3D seismic-velocity structures and seismogenic environment of the M_s 6.5 Ludian earthquake, *Bull. Seismol. Soc. Am.* **107**, no. 6, 3023–3026, doi: [10.1785/0120170072](https://doi.org/10.1785/0120170072).
- Royden, L. H., B. C. Burchfiel, R. W. King, E. Wang, Z. Chen, F. Shen, and Y. Liu (1997). Surface deformation and lower crustal flow in eastern Tibet, *Science* **276**, 788–790, doi: [10.1126/science.276.5313.788](https://doi.org/10.1126/science.276.5313.788).
- Savage, M. K. (1999). Seismic anisotropy and mantle deformation: What have we learned from shear wave splitting? *Rev. Geophys.* **37**, no. 1, 65–106, doi: [10.1029/98rg02075](https://doi.org/10.1029/98rg02075).
- Schulte-Pelkum, V., G. Masters, and P. M. Shearer (2001). Upper mantle anisotropy from long-period P polarization, *J. Geophys. Res.* **106**, no. B10, 21,917–21,934, doi: [10.1029/2001JB000346](https://doi.org/10.1029/2001JB000346).
- Shapiro, N. M., M. Campillo, L. Stehly, and M. H. Ritzwoller (2005). High-resolution surface wave tomography from ambient seismic noise, *Science* **307**, 1615–1618, doi: [10.1126/science.1108339](https://doi.org/10.1126/science.1108339).
- Shen, W., M. H. Ritzwoller, D. Kang, Y. Kim, F. Lin, J. Ning, W. Wang, Y. Zheng, and L. Zhou (2016). A seismic reference model for the crust and uppermost mantle beneath China from surface wave dispersion, *Geophys. J. Int.* **206**, 954–979, doi: [10.1093/gji/ggw175](https://doi.org/10.1093/gji/ggw175).
- Silver, P. G., and W. Chan (1991). Shear wave splitting and subcontinental mantle deformation, *J. Geophys. Res.* **96**, no. 10, 16,429–16,454, doi: [10.1029/91jb00899](https://doi.org/10.1029/91jb00899).
- Sun, X., X. Bao, M. Xu, D. W. Eaton, X. Song, L. Wang, Z. Ding, N. Mi, D. Yu, and H. Li (2014). Crustal structure beneath SE Tibet from joint analysis of receiver functions and Rayleigh wave dispersion, *Geophys. Res. Lett.* **41**, 1479–1484, doi: [10.1002/2014GL059269](https://doi.org/10.1002/2014GL059269).
- Sun, Y., F. Niu, H. Liu, Y. Chen, and J. Liu (2012). Crustal structure and deformation of the SE Tibetan plateau revealed by receiver function data, *Earth Planet. Sci. Lett.* **349**, 186–197, doi: [10.1016/j.epsl.2012.07.007](https://doi.org/10.1016/j.epsl.2012.07.007).
- Wang, L., and F. Niu (2019). Anomalous $SmKS$ induced by postcritical reflection and refraction at the core-mantle boundary, *Sci. Bull.* **64**, 1601–1607, doi: [10.1016/j.scib.2019.09.004](https://doi.org/10.1016/j.scib.2019.09.004).
- Wang, W., P. Gerstoft, and B. Wang (2018). Seasonality of P wave microseisms from NCF-based beamforming using CHINArray, *Geophys. J. Int.* **213**, 1832–1848, doi: [10.1093/gji/ggy081](https://doi.org/10.1093/gji/ggy081).
- Wang, W., J. Wu, L. Fang, G. Lai, and Y. Cai (2017). Crustal thickness and Poisson's ratio in southwest China based on data from dense seismic arrays, *J. Geophys. Res.* **122**, 7219–7235, doi: [10.1002/2017JB013978](https://doi.org/10.1002/2017JB013978).
- Wang, W., J. Wu, L. Fang, G. Lai, T. Yang, and Y. Cai (2014). S wave velocity structure in southwest China from surface wave tomography and receiver functions, *J. Geophys. Res.* **119**, 1061–1078, doi: [10.1002/2013JB010317](https://doi.org/10.1002/2013JB010317).
- Wessel, P., and W. Smith (1998). New, improved version of Generic Mapping Tools released, *Eos Trans. AGU* **79**, no. 47, 579.
- Xie, J., M. H. Ritzwoller, W. Shen, and W. Wang (2017). Crustal anisotropy across eastern Tibet and surroundings modeled as a depth-dependent tilted hexagonally symmetric medium, *Geophys. J. Int.* **209**, 466–491, doi: [10.1093/gji/ggx004](https://doi.org/10.1093/gji/ggx004).
- Xie, J., M. H. Ritzwoller, W. Shen, Y. Yang, Y. Zheng, and L. Zhou (2013). Crustal radial anisotropy across eastern Tibet and the western Yangtze craton, *J. Geophys. Res.* **118**, 4226–4252, doi: [10.1002/jgrb.50296](https://doi.org/10.1002/jgrb.50296).
- Xie, Z., B. Jin, Y. Zheng, C. Ge, X. Xiong, C. Xiong, and H. HouTze (2013). Source parameters inversion of the 2013 Lushan earthquake by combining teleseismic waveforms and local seismograms, *Sci. China Earth Sci.* **56**, 1177–1186, doi: [10.1007/s11430-013-4640-3](https://doi.org/10.1007/s11430-013-4640-3).
- Yang, Y., M. H. Ritzwoller, Y. Zheng, W. Shen, A. L. Levshin, and Z. Xie (2012). A synoptic view of the distribution and connectivity of the mid-crustal low velocity zone beneath Tibet, *J. Geophys. Res.* **117**, no. B04303, doi: [10.1029/2011JB008810](https://doi.org/10.1029/2011JB008810).
- Yang, Y., Y. Zheng, J. Chen, S. Zhou, S. Celyan, E. Sandvol, F. Tilmann, K. Priestley, T. M. Hearn, J. F. Ni, *et al.* (2010). Rayleigh wave phase velocity maps of Tibet and the surrounding regions from ambient seismic noise tomography, *Geochem. Geophys. Geosys.* **11**, no. Q08010, doi: [10.1029/2010GC003119](https://doi.org/10.1029/2010GC003119).
- Yao, H., C. Beghein, and R. D. van der Hilst (2008). Surface wave array tomography in SE Tibet from ambient seismic noise and two-station analysis—II. Crustal and upper-mantle structure, *Geophys. J. Int.* **173**, 205–219, doi: [10.1111/j.1365-246X.2007.03696.x](https://doi.org/10.1111/j.1365-246X.2007.03696.x).
- Yin, A. (2010). Cenozoic tectonic evolution of Asia: A preliminary synthesis, *Tectonophysics* **488**, 293–325, doi: [10.1016/j.tecto.2009.06.002](https://doi.org/10.1016/j.tecto.2009.06.002).
- Zha, Y., S. C. Webb, and W. Menke (2013). Determining the orientations of ocean bottom seismometers using ambient noise correlation, *Geophys. Res. Lett.* **40**, 3585–3590, doi: [10.1002/grl.50698](https://doi.org/10.1002/grl.50698).
- Zhang, F. X., Q. Wu, Y. Li, R. Zhang, L. Sun, J. Pan, and Z. Ding (2018). Seismic tomography of eastern Tibet: Implications for the Tibetan plateau growth, *Tectonics* **37**, 2833–2847, doi: [10.1029/2018TC004977](https://doi.org/10.1029/2018TC004977).
- Zhang, P. (2013). A review on active tectonics and deep crustal processes of the Western Sichuan region, eastern margin of the Tibetan Plateau, *Tectonophysics* **584**, 7–22, doi: [10.1016/j.tecto.2012.02.021](https://doi.org/10.1016/j.tecto.2012.02.021).
- Zhang, P., and E. B. Engdahl (2013). Great earthquakes in the 21st century and geodynamics of the Tibetan Plateau, *Tectonophysics* **584**, 1–6, doi: [10.1016/j.tecto.2012.11.001](https://doi.org/10.1016/j.tecto.2012.11.001).
- Zheng, C., R. Zhang, Q. Wu, Y. Li, F. Zhang, K. Shi, and Z. Ding (2019). Variations in crustal and uppermost mantle structures across eastern Tibet and adjacent regions: Implications of crustal flow and asthenospheric upwelling combined for expansions of the Tibetan plateau, *Tectonics* **38**, 3167–3181, doi: [10.1029/2018TC005276](https://doi.org/10.1029/2018TC005276).
- Zheng, X., B. Ouyang, D. Zhang, Z. Yao, J. Liang, and J. Zheng (2009). Technical system construction of Data Backup Centre for China Seismograph Network and the data support to researches on the Wenchuan earthquake, *Chin. J. Geophys.* **52**, no. 5, 1412–1417, doi: [10.3969/j.issn.0001-5733.2009.05.031](https://doi.org/10.3969/j.issn.0001-5733.2009.05.031) (in Chinese with English abstract).
- Zhu, L., and H. Kanamori (2000). Moho depth variation in southern California from teleseismic receiver functions, *J. Geophys. Res.* **105**, 2969–2980, doi: [10.1029/1999JB900322](https://doi.org/10.1029/1999JB900322).

Manuscript received 24 March 2020
Published online 6 October 2020